Bioactive Materials 24 (2023) 124–135

Contents lists available at ScienceDirect

Bioactive Materials

journal homepage: www.keaipublishing.com/en/journals/bioactive-materials

# *In vitro* and *in vivo* evaluation of cerium oxide nanoparticles in respiratory syncytial virus infection

Akhil Patel [a,1], Jessica Kosanovich [a,1], Sameera Sansare [a], Sricharani Balmuri [a], Vinayak Sant [a], Kerry M. Empey [a,b,**], Shilpa Sant [a,c,*]

[a] Department of Pharmaceutical Sciences, School of Pharmacy, University of Pittsburgh, Pittsburgh, PA, 15261, USA
[b] Center for Clinical Pharmaceutical Sciences, Department of Pharmacy and Therapeutics, School of Pharmacy, Clinical and Translational Science Institute, Department of Immunology, School of Medicine, University of Pittsburgh, Pittsburgh, PA, 15261, USA
[c] Department of Bioengineering, Swanson School of Engineering, McGowan Institute for Regenerative Medicine, UPMC Hillman Cancer Center, University of Pittsburgh, Pittsburgh, PA, 15261, USA

ARTICLE INFO

*Keywords:*
Cerium oxide nanoparticles
Reactive oxygen species
Respiratory syncytial virus
Macrophage phenotypes
Immunomodulation
Nanoparticle shape
Bioactive nanoparticles

ABSTRACT

Respiratory syncytial virus (RSV) is the most common cause of viral bronchiolitis among children worldwide, yet there is no vaccine for RSV disease. This study investigates the potential of cube and sphere-shaped cerium oxide nanoparticles (CNP) to modulate reactive oxygen (ROS) and nitrogen (RNS) species and immune cell phenotypes in the presence of RSV infection *in vitro* and *in vivo*. Cube and sphere-shaped CNP were synthesized by hydrothermal and ultrasonication methods, respectively. Physico-chemical characterization confirmed the shape of sphere and cube CNP and effect of various parameters on their particle size distribution and zeta potential. *In vitro* results revealed that sphere and cube CNP differentially modulated ROS and RNS levels in J774 macrophages. Specifically, cube CNP significantly reduced RSV-induced ROS levels without affecting RNS levels while sphere CNP increased RSV-induced RNS levels with minimal effect on ROS levels. Cube CNP drove an M1 phenotype in RSV-infected macrophages *in vitro* by increasing macrophage surface expression of CD80 and CD86 with a concomitant increase in TNFα and IL-12p70, while simultaneously decreasing M2 CD206 expression. Intranasal administration of sphere and cube-CNP were well-tolerated with no observed toxicity in BALB/c mice. Notably, cube CNP preferentially accumulated in murine alveolar macrophages and induced their activation, avoiding enhanced uptake and activation of other inflammatory cells such as neutrophils, which are associated with RSV-mediated inflammation. In conclusion, we report that sphere and cube CNP modulate macrophage polarization and innate cellular responses during RSV infection.

## 1. Introduction

Respiratory viruses are a major cause of mortality worldwide, with an estimated 2.7 million deaths reported in a single year [1]. As of September 13, 2021, the World Health Organization has reported over 4.6 million deaths due to SARS-CoV2 alone, a number which is continuing to rise. This emerging pathogen joins the ranks of other deadly viruses, such as influenza, which claims the lives of up to 200,000 people annually and respiratory syncytial virus (RSV), which kills approximately 18,000 people each year [2]. In the US, annual RSV infection leads to ~1.5 million outpatient visits among children <5 years of age with up to 125,000 estimated RSV-related hospitalizations

*Abbreviations:* CNP, Cerium oxide nanoparticles; RSV, Respiratory syncytial virus; Gas6, Growth arrest specific-6; ROS, Reactive oxygen species; RNS, Reactive nitrogen species; BHA, Butylated hydroxyanisole; HEPES, 4-(2-hydroxyethyl)-1-piperazineethanesulfonic acid; SOD, Superoxide dismutase; TEM, Transmission electron microscopy; FITC, Fluorescein isothiocyanate; DLS, Dynamic light scattering; MFI, Mean fluorescence intensity; PBS, Phosphate buffered saline; DMEM, Dulbecco's Modified Eagle's Medium; BAL, Bronchoalveolar lavage; RFU, Relative fluorescence units; iNOS, Induced nitrous oxide synthase; APTES, 3-aminopropyltriethoxysilane; SDS-PAGE, Sodium dodecyl sulfate polyacrylamide gel electrophoresis.

Peer review under responsibility of KeAi Communications Co., Ltd.

* Corresponding author. 700 Technology Drive, Pittsburgh Technology Center, Room 4307, Pittsburgh, PA, 15219, USA.
** Corresponding author. 3501 Terrace Street, 207 Salk Pavilion, Pittsburgh, PA, 15261, USA.
*E-mail addresses:* kme33@pitt.edu (K.M. Empey), shs149@pitt.edu (S. Sant).
[1] Authors contributed equally to the work.

https://doi.org/10.1016/j.bioactmat.2022.12.005
Received 14 August 2022; Received in revised form 23 November 2022; Accepted 6 December 2022

in children <1 year of age. Despite the global burden of the RSV disease, there is no approved RSV vaccine; however, prophylactic monoclonal antibody therapeutics, such as Synagis from MedImmune (palivizumab), are available for high-risk infants [3]. Severe RSV infection is associated with bronchiolar obstruction, air trapping, and emphysema due to excess mucus secretion, apoptotic cellular debris, and inflammatory cell recruitment [4,5]. Furthermore, RSV infection upregulates growth arrest specific-6 (Gas6), which induces conversion of macrophages to an M2-like phenotype, thereby increasing the susceptibility of patients to secondary bacterial infections such as pneumococcal infection [6]. While each pulmonary virus elicits a unique immune response to contain viral spread, a common factor among most pulmonary viruses is the inherent cost to mounting a robust immune response – tissue damage and immunopathology. Thus, a therapeutic strategy that mitigates tissue damaging immune responses without sacrificing antiviral activity is desperately needed.

Mounting evidence suggests that optimum levels of reactive species (oxygen and nitrogen) are important to maintain physiological redox balance [7] and to aid in viral clearance. Notably, optimum level of reactive oxygen species (ROS) triggers a signaling cascade that modulates redox-sensitive genes regulating immune and proinflammatory response, whereas elevated levels of ROS induce inflammation and tissue damage [8,9]. RSV infection induces oxidative stress, which is further enhanced by RSV-induced transcriptional inhibition of antioxidant enzymes [10,11]. A hallmark of severe pulmonary viral infections is an increase in ROS [12,13]. and thus, targeting ROS is being explored as a potential therapeutic strategy. Several studies have demonstrated that antioxidant treatment with butylated hydroxyanisole (BHA) or resveratrol and the mitochondrial ROS scavenger mitoquinone mesylate, reduced levels of peroxidation products and ameliorated clinical illness [14–18].

We have recently synthesized antioxidant cerium oxide nanoparticles (CNP) in various shapes [19,20] and have demonstrated their ROS-scavenging activity to mitigate oxidative stress-induced calcification in patient-derived primary valve interstitial cells [20]. We have also shown that such ROS-scavenging activity of CNP is dependent on their shape. CNP have demonstrated about 9-fold greater antioxidant activity compared to commercial antioxidant Trolox [21], garnering interest in the therapeutic potential of CNP to modulate oxidative stress in various diseases [22]. CNP are known to scavenge ROS through their superoxide dismutase (SOD)-mimetic or antioxidant catalase-mimetic ability of trivalent cerium ($Ce^{3+}$) [20,23]. The ROS-scavenging activity of CNP is directly proportional to oxygen vacancies on their surface ($Ce^{3+}/Ce^{4+}$ state). Moreover, these crystalline nanoparticles are proven safe in preclinical studies, and can be tolerated for doses up to 100 mg/kg for 10 days in male rats [20,24–26]. Given the importance of balanced levels of

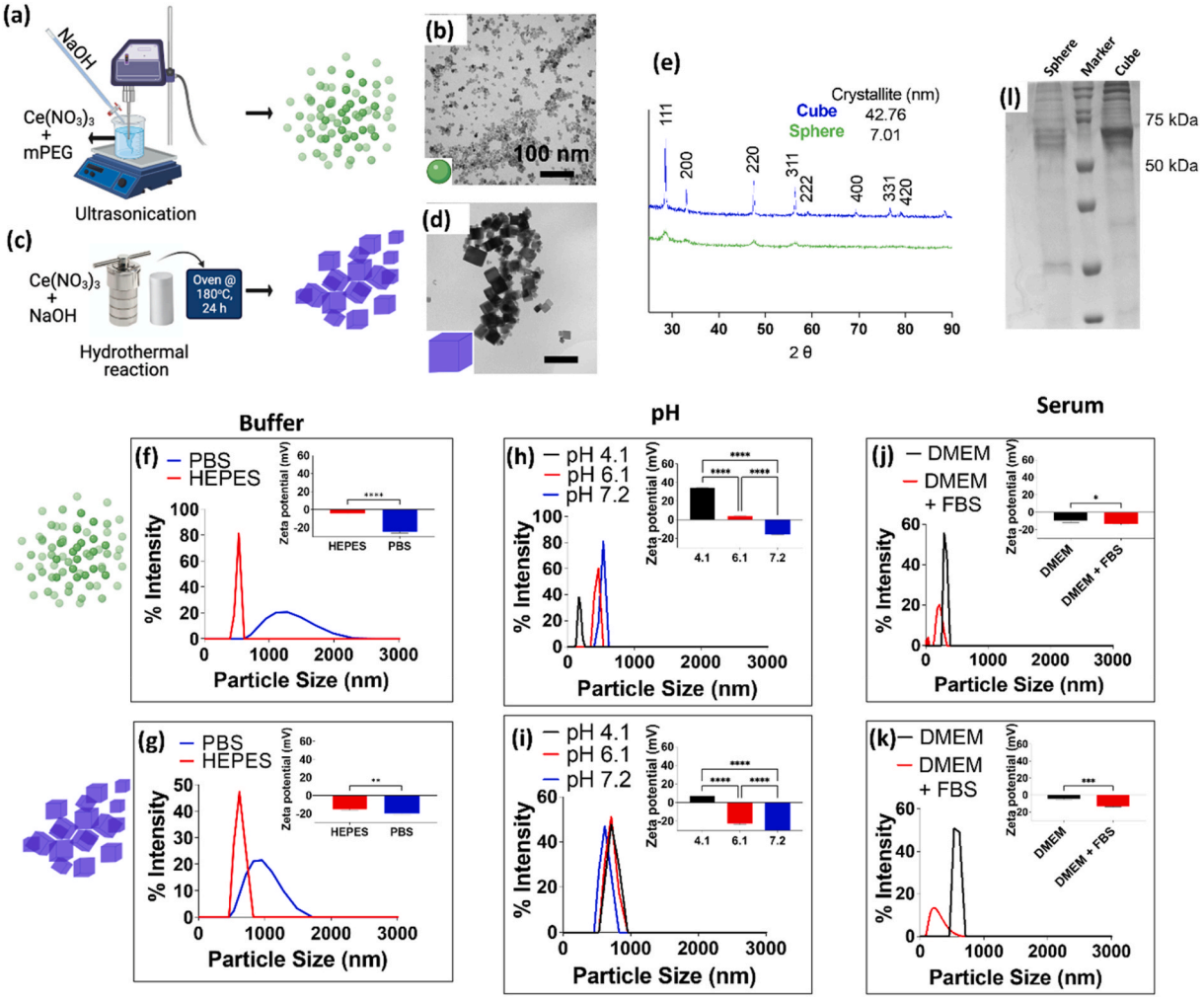


**Fig. 1. Synthesis and physicochemical characterization of Cerium oxide nanoparticles (CNP).** Schematic representation of synthesis of sphere CNP using ultrasonication method **(a)** and cube CNP using hydrothermal method **(c)**. Transmission electron microscopy images of sphere CNP **(b)** and cube CNP **(d)**; Scale bars represent 100 nm. X-ray diffraction spectra of sphere and cube CNP with crystallite quantified using Scherrer equation **(e).** Effect of buffers (PBS and HEPES) on hydrodynamic size and zeta potential of sphere CNP **(f)** and cube CNP **(g)**. Effect of pH on hydrodynamic size and zeta potential of sphere CNP **(h)** and cube CNP **(i).** Effect of serum on hydrodynamic size and zeta potential of sphere CNP (j) and cube CNP (k). SDS-PAGE of separated proteins from sphere and cube CNP (l).

reactive species for mounting robust immune response to contain viral spread without eliciting tissue damage and immunopathology, we tested the potential of sphere and cube CNP in modulating ROS and reactive nitrogen species (RNS) levels, macrophage phenotype and innate cellular responses during RSV infection *in vitro* and *in vivo*.

## 2. Results and discussion

### 2.1. Sphere and cube cerium oxide nanoparticles (CNP) exhibit distinct physicochemical properties

Differences in the shape, surface area, and dimensions of nanoparticles are known to affect various properties such as catalytic performance of CNP [27]. The sphere CNP were synthesized by ultrasonication method (Fig. 1a), whereby colloidal nanocrystals formed in the first step of the reaction adsorb hydroxyl ions to form spherical nanocrystals. Transmission electron microscopy (TEM) micrographs confirmed the shape of sphere CNP with an average diameter of 11.3 nm (Fig. 1b). The cube CNP were synthesized by hydrothermal method (Fig. 1c) and their shape was confirmed by TEM (Fig. 1d) with an average dimension of 19.3 nm. Formation of nanocube CNP can be explained by higher temperatures achieved in the hydrothermal reactor under high pressure for 24 h. This allows oxidation of the intermediate nanocrystals such as nanorods and nanotubes, which further coarsen to form cube morphology through Ostwald ripening [28]. Catalytic power of CNP is known to be shape-specific because of differences in highly reactive exposed crystal planes. Mai *et al.* have shown that crystalline cube CNP contain more highly reactive exposed crystal planes compared to other shapes [29]. Therefore, we characterized crystalline properties of CNP using X-ray diffraction (XRD). Sphere CNP showed a moderately crystalline phase whereas cube CNP showed a highly crystalline phase as evident from sharp peaks in XRD spectra (Fig. 1e). Crystallite calculation through Scherrer equation [30] showed six-fold higher crystallite size for cube CNP compared to sphere CNP indicating larger size. Additionally, presence of higher intensity peaks in the XRD spectra of cube CNP indicates relatively more crystalline and stable nanocrystal form for cube CNP as compared to sphere CNP.

To identify an optimum suspension medium for CNP, we studied the effect of 4-(2-hydroxyethyl)-1-piperazineethanesulfonic acid (HEPES) buffer (non-ionizable buffer system) and phosphate buffered saline (PBS) (ionizable buffer system) on the hydrodynamic size and zeta potential of CNP. Sphere CNP showed an average hydrodynamic size of 676 ± 55 nm in HEPES at pH 7.2 and 1228 ± 78 nm in PBS, whereas cube CNP showed an average hydrodynamic size of 561 ± 73 nm and 905 ± 37 nm in HEPES pH 7.2 and PBS, respectively **(**Supplementary Tables 1 and 2**).** Dynamic light scattering (DLS) measurements showed narrow size distribution for sphere (Fig. 1f) and cube (Fig. 1g) CNP in HEPES buffer, while both CNP showed a broad particle size distribution in PBS suggesting that the ionic strength can affect the aggregation behavior of sphere and cube CNP. Indeed, Qi *et al.* [31] have shown that the long-range electrostatic forces and short-range hydration interactions play a critical role in the stability of CNP in a suspension, where an increase in the ionic strength or pH resulted in reversible aggregation of CNP. Both, sphere and cube CNP showed negative zeta potential in HEPES and PBS.

Since both sphere and cube CNP showed less aggregation in HEPES buffer compared to PBS, we next assessed the effect of pH (4.1, 6.1 and 7.2) on CNP size and zeta potential using HEPES buffer. At pH 4.1, sphere CNP showed high positive zeta potential and hydrodynamic size of 182 ± 14 nm (Fig. 1h, Supplementary Tables 1 and 2). Sphere CNP showed larger aggregates and zeta potential close to zero at pH 6.1, and negative zeta potential at pH 7.2. The cube CNP showed minimal effect of pH with similar hydrodynamic size in the range of 500–700 nm throughout 4.1–7.2 pH, while their zeta potential switched from 6.9 ± 0.5 at 4.1 to −31.2 ± 0.6 as pH increased to 7.2 (Fig. 1i, (Supplementary Tables 1 and 2). These pH-dependent changes in zeta potential and size could be attributed to the changes in the isoelectric point of CNP that are dependent of the suspension medium and synthesis methodology [32].

To determine the effect of protein adsorption, we measured size and zeta potential of CNP in Dulbecco's Modified Eagle's Medium (DMEM) with and without (10% v/v) fetal bovine serum. Both sphere (Fig. 1j) and cube CNP (Fig. 1k) showed significant reduction in average particle size as well as zeta potential in presence of serum. This could be attributed to stabilization of CNP suspension by adsorption of serum proteins or steric hindrance, which would be beneficial under physiological conditions to prevent aggregation *in vivo* in the presence of serum proteins [33]. Comparison of protein adsorption by SDS-PAGE revealed comparatively higher protein adsorption in cube CNP compared to sphere CNP (Fig. 1l).

Taken together, despite differences in shape and crystallinity of sphere and cube CNP, similar suspension characteristics (size and zeta potential) were observed in the presence of serum proteins (Fig. 1j and k, Supplementary Tables 1 and 2).

### 2.2. Sphere and cube CNP are readily taken up by J774A.1 macrophages in vitro

To determine the potential cytotoxicity of sphere and cube CNP, the viability of J774A.1 macrophage cells exposed to increasing concentration of CNP was assessed using an Alamar Blue assay. Metabolic activity of macrophages with CNP treatment was compared with macrophages without CNP treatment to calculate percentage viability. Both sphere and cube CNP demonstrated greater than 80% viability for doses up to 150 μg/mL (Fig. 2a). To investigate if CNP were taken up by J774A.1 macrophages, cellular uptake of fluorescein isothiocyanate (FITC)-labeled CNP was analyzed by confocal imaging. After 6 h of incubation, the sphere CNP (Fig. 2b1-b3) and cube CNP (Fig. 2c1-c3) were readily taken up by macrophages. Both CNP were localized in the cytosol of the macrophages (Fig. 2b4 2b5, 2c4, 2c5). Confocal image analysis further showed significantly higher mean fluorescence intensity (MFI) for cube CNP compared to sphere CNP confirming qualitative observations and indicating higher macrophage uptake of cube CNP (Fig. 2d). Cube CNP showed higher crystallinity, which taken together with its higher catalytic reactivity established previously by Mai *et al.* [29], could exhibit greater interaction with macrophages relative to sphere CNP.

### 2.3. Sphere and cube CNP trigger differential ROS and RNS levels in RSV-infected macrophages

Increased ROS level is one of the hallmarks of RSV infection, which leads to tissue damage and airway inflammation [13,34–36]. To evaluate the potential of CNP to alter redox microenvironment, we developed an *in vitro* assay where virus-free J774A.1 macrophages or macrophages infected with RSV L19 were subsequently treated with sphere or cube CNP. We measured the ability of sphere and cube CNP to modulate reactive oxygen and nitrogen species in J774A1 macrophages in the absence or presence of RSV infection. ROS levels were measured in live cells using CellROX® fluorogenic microplate assay. The CellROX® reagent is weakly fluorescent and changes to bright green color under oxidized state in the presence of ROS. Neither sphere nor cube CNP significantly altered ROS levels in uninfected and RSV-infected macrophages after 6 h nanoparticle treatment (Fig. 3a). After 12 h, RSV infection induced significantly higher ROS production (~$6 \times 10^5$ RFU/mg protein, red bar) in infected macrophages compared to uninfected macrophages (black bar) (Fig. 3b). Interestingly, 12 h treatment of RSV-infected macrophages with cube CNP (blue striped bar) significantly reduced RSV-induced increase in ROS levels. This may suggest the potential of cube CNP to reduce tissue damage through reduction of ROS levels in RSV-infected macrophages. Although not statistically significant, a similar trend was observed with sphere CNP treatment in RSV-infected macrophages (green striped bar), highlighting the ability

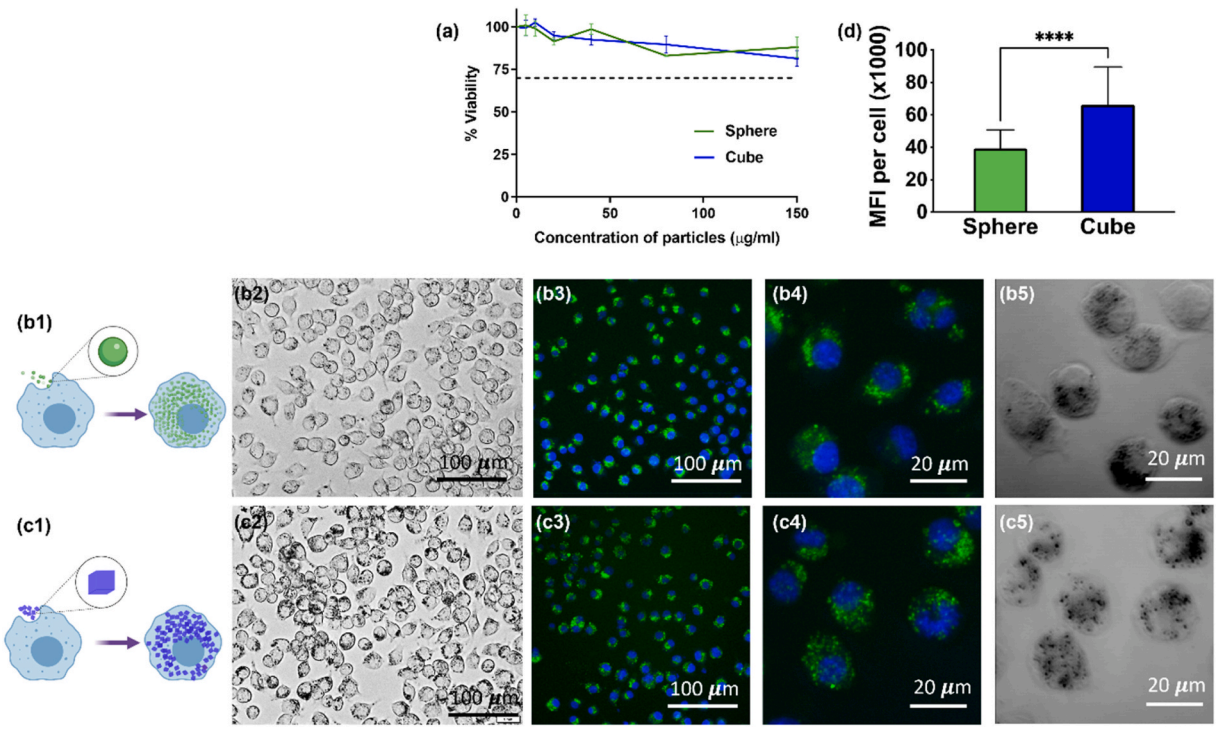


**Fig. 2. Sphere and cube CNP are readily taken up by J774A.1 macrophages *in vitro*.** Percentage cell viability of J774A.1 macrophages after 24 h incubation with sphere and cube CNP at various concentrations (a). Schematic representation of *in vitro* uptake of sphere CNP (b1) and cube CNP (c1) by J774A.1 macrophages. DIC images of J774A.1 macrophages after 6 h of incubation with sphere CNP (b2) and cube CNP (c2); Scale bar represents 100 μm. Confocal images with multiple z-stacks showing uptake of FITC-sphere (b3, b4) and FITC-cube CNP (c3, c4) at different magnifications; green channel indicates FITC-tagged CNP and blue channel indicates HOECHST-stained nuclei of macrophages. Confocal images with DIC channel showing macrophage boundaries and sphere CNP (b5) or cube CNP (c5). Mean fluorescent intensity (x1000) calculated from confocal images (d). An unpaired *t*-test was used to compare groups. ****$p < 0.0001$.

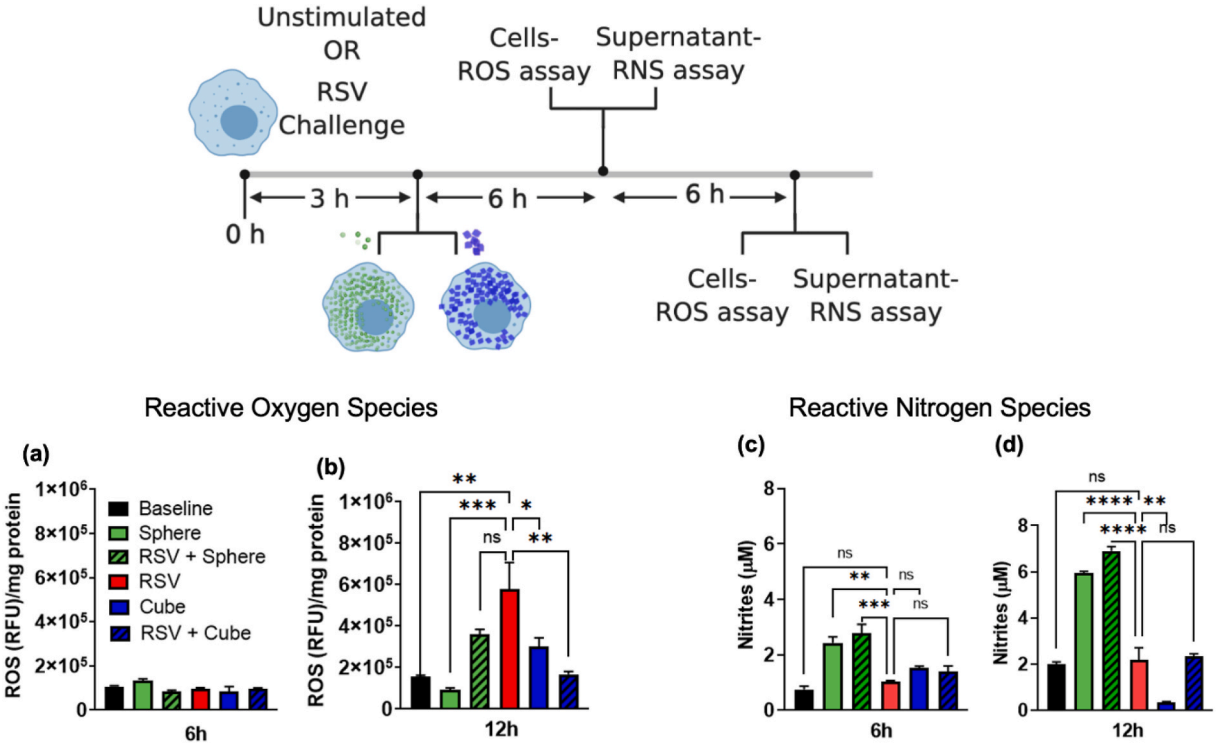


**Fig. 3. Sphere and cube CNP trigger differential ROS and RNS levels in RSV-infected macrophages.** Measurement of reactive oxygen species using CellROX assay following RSV infection with or without CNP for 6 or 12 h (a, b). Measurement of reactive nitrogen species using Griess reagent assay following RSV infection with or without CNP for 6 or 12 h (c, d). Data are represented as mean ± SEM. A one-way ANOVA with Tukey's multiple comparison post-hoc test was used to compare groups. *$p < 0.05$; **$p < 0.01$; ***$p < 0.001$; ****$p < 0.0001$ compared to RSV-infected macrophages.

of both sphere and cube CNP to decrease RSV-induced ROS production. In our previous study, sphere CNP scavenged acute ROS generated by hydrogen peroxide treatment in valvular interstitial cells in a dose-dependent manner whereas pretreatment of cube CNP to hydrogen peroxide challenge prevented increase in ROS levels [20]. Such free radical scavenging activity of CNP is exerted through their superoxide dismutase-mimetic mechanism [23].

RNS are known to be the fulcrum that shifts the macrophage polarity from pro-inflammatory (M1) to regenerative (M2) states [37–39]. Optimal extracellular RNS level is important to enable cytotoxic activity of macrophages [37]. Unlike ROS generated within the cytoplasm of the macrophages, RNS is generated extracellularly from rapid diffusion of nitric oxide (NO) out of cell membrane [40]. Nitric oxide reacts with other oxygen species in the extracellular medium producing RNS, which are relatively more stable compared to short-lived nitric oxide. Extracellular RNS, together with induced nitrous oxide synthase (iNOS) enzyme, provide protection and eradicate pathogens such as *Mycobacterium tuberculosis* [41]. RSV infection is known to alter homeostatic

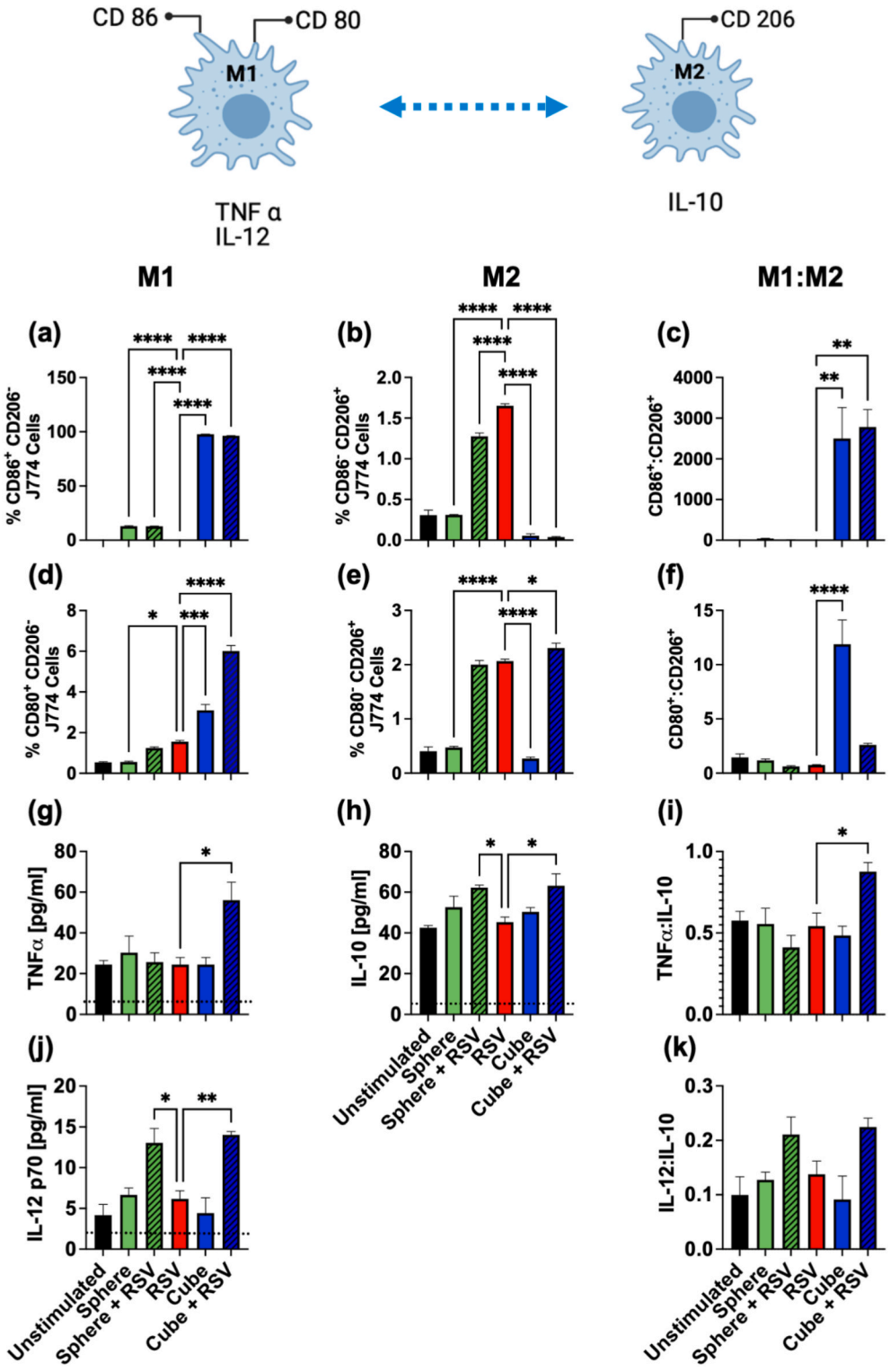


**Fig. 4. CNP alter macrophage phenotypes in the presence of RSV infection.** J774A.1 macrophages were infected with RSV Line19 at a multiplicity of infection (MOI) of 3 for 3 h prior to treatment with sphere or cube CNP. At 6 h post-nanoparticle treatment, percent of macrophages with the phenotypes $CD86^{+}CD206-$ (a), $CD86^{-}CD206+$ (b), $CD80^{+}CD206-$ (d) and $CD80^{-}CD206+$ (e) were quantified via flow cytometry. Ratio of CD86+:CD206+ (c) and CD80+:CD206+ (f) macrophages were calculated for each group. At 24 h post-nanoparticle treatment, TNFα (g), IL-10 (h), and IL-12p70 (j) cytokine levels were measured from cell supernatants via Luminex. Ratios of TNFα:IL-10 (i) and IL-12p70:IL-10 (k) were calculated for each group. Data are represented as mean ± SEM. A one-way ANOVA with Dunnett's multiple comparison post-test was used to compare groups with RSV infection and each treatment condition. *$p < 0.05$, **$p < 0.01$, ***$p < 0.001$, and ****$p < 0.0001$. The dotted lines in g, h, and j indicate the lower limit of quantification.

levels of NO and RNS primarily through iNOS induction. Therefore, we measured the extracellular RNS levels using Griess reagent in CNP-treated virus-free and RSV-infected macrophages (Fig. 3c and d). At 6 h, sphere CNP treatment of RSV-infected macrophages (green striped bar) significantly increased RSV-induced RNS levels (red bars) (Fig. 3c). These higher RNS levels sustained 12 h post-RSV infection in sphere CNP-treated RSV-infected macrophages (Fig. 3d). Cube CNP treatment (blue striped bar), however, did not alter RSV-induced RNS levels at 6 and 12 h, further highlighting differential CNP responses in modulating extracellular RNS levels in RSV-infected macrophages. Such differential response in RNS modulation was also evident in virus-free macrophages treated with CNP for 12 h. Specifically, sphere CNP increased and cube CNP reduced RNS levels significantly in virus-free macrophages compared to untreated RSV-infected macrophages at 12 h (Fig. 3d).

Collectively, cube CNP reduced RSV-induced ROS levels significantly without affecting RNS levels while sphere CNP increased RSV-induced RNS levels with minimal effect on ROS levels, suggesting that physicochemical properties of CNP can be a critical driver of differential cellular ROS and RNS levels *in vitro*.

### 2.4. CNP alter macrophage phenotypes in the presence of RSV infection in vitro

The reduction of ROS levels and optimal RNS levels are beneficial to prevent tissue damage in lungs [8]. Therefore, to investigate the impact of differential ROS and RNS levels generated by CNP on RSV-infected macrophage phenotype, we characterized surface markers and cytokines secreted by virus-free and RSV-infected macrophages treated with sphere and cube CNP. To evaluate the potential of CNP to polarize macrophage phenotype, surface expression of M1 markers (CD86 and CD80) and the M2 marker (CD206) were measured 6 h post-CNP treatment via flow cytometry. RSV infection alone (red bars) failed to increase the frequency of M1 macrophages (Fig. 4a and b, Supplemental Fig. 1), while treatment of uninfected and RSV-infected macrophages with sphere and cube CNP increased the frequency of M1 $CD86^+$ $CD206^-$ J774A.1 macrophages. The increased M1 macrophage phenotype ($CD86^+$ $CD206^-$) was predominantly driven by the CNP irrespective of infection status as reflected by the ~12% increase in sphere-treated macrophages and ~96% increase in cube-treated macrophages (Fig. 4a, Supplemental Fig. 1). On the other hand, sphere and cube CNP reduced the frequency of M2 $CD86^-$ $CD206^+$ macrophages in both uninfected and RSV-infected macrophages relative to RSV infection alone (Fig. 4b, Supplemental Fig. 1). These results suggest that CNP influenced RSV-associated macrophage activation where cube CNP favored a more anti-viral M1 phenotype compared to sphere CNP at 6 h post-treatment (Fig. 4c). Consistent with Fig. 4a, the use of CD80 as an alternative M1 marker showed that cube CNP increased the frequency of M1 macrophages, but sphere CNP did not (Fig. 4d). Similarly, only Cube + RSV increased M2 $CD80^-$ $CD206^+$ macrophages (Fig. 4e, Supplemental Fig. 2). A comparison of the $CD80^+$ M1 to M2 phenotype showed greater frequency of the anti-viral M1 *versus* M2 macrophage phenotype with cube CNP ($CD80^+$:$CD206^+$ ratio) when compared to RSV alone (Fig. 4f, Supplemental Fig. 2).

Given the ability of CNP to alter the surface expression of M1 and M2 macrophage markers, we next assessed macrophage function by measuring cytokine production following treatment with sphere or cube CNP in uninfected and RSV-infected macrophages. Consistent with the dominant M1 phenotype shown in Fig. 4a–f, cube CNP led to a significant increase in the production of TNFα, an M1-associated cytokine in RSV-infected macrophages (Fig. 4g). Interestingly, both sphere and cube CNP induced a modest increase in the M2-associated cytokine IL-10 (Fig. 4h), which functions to prevent excess inflammation. A ratio of TNFα to IL-10 (Fig. 4i) indicates that cube, but not sphere CNP favored the anti-viral TNFα response at the 24 h time point in RSV-infected macrophages as compared to untreated macrophages (red bars). Cube CNP also induced a significant increase in the production of IL-12p70, an additional M1-associated cytokine in RSV-infected macrophages relative to untreated macrophages (Fig. 4j). Unlike TNFα, an increase in IL-12p70 was also noted with sphere CNP in RSV-infected macrophages (Fig. 4j). Although non-significant, cube CNP induced an increase in ratio of IL-12p70 to IL-10 in RSV-infected macrophages (Fig. 4k). Taken together, cube CNP drove an M1 phenotype by increasing macrophage surface expression of CD80 and CD86 with a concomitant increase in TNFα and IL-12p70, while simultaneously decreasing M2 CD206 expression.

CD80 and CD86 provide critical co-stimulation signals for the full activation and functional responses of T cells [42]. The higher expression of CD80 and CD86 in cube CNP-treated macrophages is indicative of a phenotype shift aligned with the ability to effectively stimulate anti-viral T cells, which are known to protect against RSV infection [43]. Consistent with previously published data, these data confirm that RSV infection favors an M2 macrophage phenotype in the J774A.1 mouse macrophage cell line [44]. In our previous work, we show that the M2 phenotype can be overcome with the addition of anti-viral IFNγ resulting in reduced viral titers and greater iNOS [44]. Similarly, *in vivo* work confirmed that IFNγ treatment of RSV-infected BALB/c mice significantly induced alveolar macrophage activation and reduced viral titers [45]. However, the use of inhaled IFNγ as a clinical therapeutic option is limited by the risk of inducing extensive inflammation in the infant airway. These data suggest that the use of cube CNP offers a feasible alternative to activation of macrophages in a more controlled and balanced manner.

### 2.5. Intranasal administration of CNP is safe

To translate our findings to an *in vivo* model and to assess CNP safety, adult mice were intranasally infected with RSV L19 and treated with two intranasal doses of sphere or cube CNP at 1- and 3-days post-infection

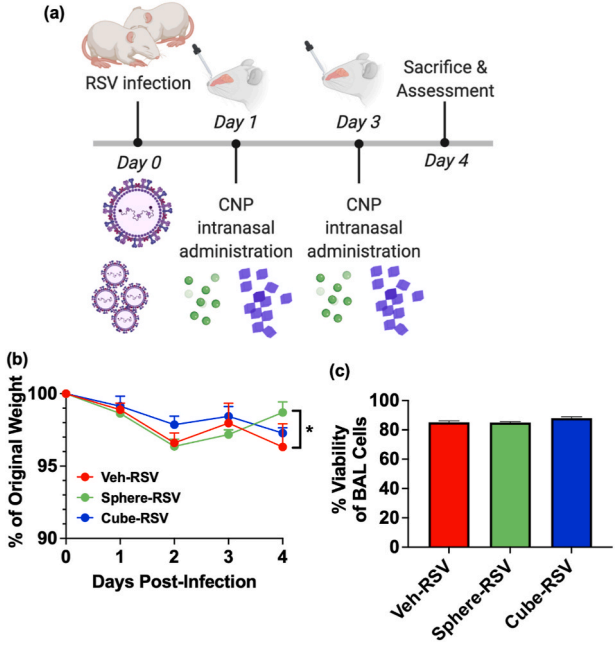


**Fig. 5. Intranasal administration of CNP is safe.** 8-week-old Balb/c mice were intranasally infected with $5 \times 10^5$ PFU/g of RSV Line19. At 1- and 3-days post-infection, mice received 55μg/100 μL dose of sphere or cube CNP or were administered 10 mM HEPES as a vehicle control (a). Weight was measured daily before and throughout infection and is represented as % of original weight (b). At 4 days post-infection, bronchoalveolar lavage (BAL) cells were assessed for viability (c). Data are represented as mean ± SEM. A two-way ANOVA (b) or a one-way ANOVA (c, d) with Tukey's multiple comparison post-test was used to compare groups.

(Fig. 5a). As expected, mice in all 3 groups lost weight at 2 days post-infection, which is attributed to early M1 cytokine release following RSV infection [46]. By 4 days post-infection, mice that received sphere CNP had lost significantly less weight than untreated mice and cube CNP appeared to have less overall weight loss at each day through 4 days post-infection (Fig. 5b). Moreover, treatment with sphere or cube CNP did not reduce the viability of cells retrieved from the bronchoalveolar lavage (BAL) fluid (Fig. 5c), suggesting that both sphere and cube CNP are safe in mice in the doses given. Taken together, these results suggest that *in vivo* administration of both sphere and cube CNP is safe at the doses used in these studies. It is important to note, however, that RSV-mediated disease pathology is primarily driven by the host immune response to RSV, rather than viral-mediated cellular destruction [47]. Thus, a treatment option that is safe and can subvert excess inflammation, such as CNP, may be ideally suited to treat the severe inflammation associated with RSV disease.

### 2.6. CNP lead to differential uptake by immune cells in murine lungs

Next, we assessed innate immune cell infiltration into the

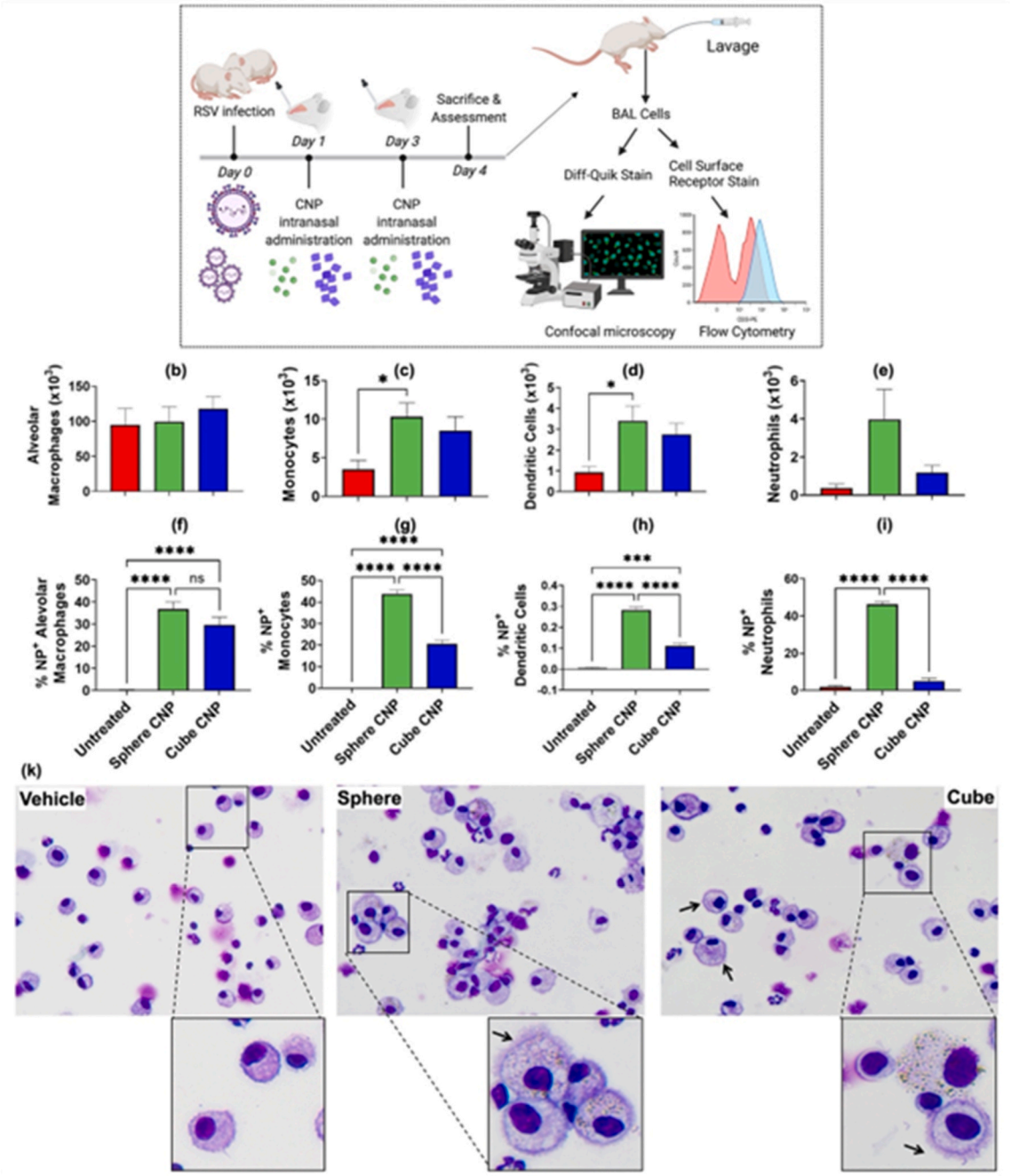


**Fig. 6. CNP lead to differential uptake by immune cells in murine lungs.** Mice were infected and treated as previously described. At 4 days post-infection, total alveolar macrophages (b), monocytes (c), dendritic cells (d), and neutrophils (e) were quantified in the BAL of infected animals via flow cytometry. The percentage of nanoparticle uptake by alveolar macrophages (f), monocytes (g), dendritic cells (h), and neutrophils (i) was measured via flow cytometry. Cytospins of alveolar macrophages obtained from BAL were imaged to assess cell morphology changes as a result of sphere or cube CNP treatment (k). Black arrows indicate activated macrophage morphology. Data are represented as mean ± SEM. A one-way ANOVA with Tukey's multiple comparison post-test was used to compare groups. *$p < 0.05$, ***$p < 0.001$, and ****$p < 0.0001$.

bronchoalveolar lavage (BAL) of RSV-infected animals following administration of either sphere or cube CNP, as described in Fig. 6a. Treatment with sphere or cube CNP following intranasal RSV infection did not alter the number of alveolar macrophages in the airspace (Fig. 6b, Supplemental Figs. 3a–c). However, treatment with sphere CNP (green bar), but not cube CNP (blue bar), significantly increased the recruitment of monocytes (Fig. 6c, Supplemental Figs. 4a–c) and dendritic cells (Fig. 6d, Supplemental Figs. 5a–c) to the airspace when compared to untreated animals. Since dendritic cells are a primary antigen presenting cell, these data suggest that the increased dendritic cell numbers in the sphere CNP group may result in greater dendritic cell-mediated T cell activation. Additionally, there was a non-significant trend toward increased neutrophil infiltration in sphere CNP-treated animals compared to untreated and cube CNP groups (Fig. 6e, Supplemental Figs. 6a–c), suggesting a differential recruitment of inflammatory cells to the airway specific to sphere and cube CNP; lack of significance in this data is likely due to variability in the sphere CNP group. Using FITC-labeled CNP, we next assessed the uptake of CNP by the various immune cell populations present in the BAL. The percentage of alveolar macrophages that phagocytosed nanoparticles was not significantly different between sphere and cube CNP-treated animals (Fig. 6f, Supplemental Figs. 3d–f) unlike higher uptake observed for cube CNP in J774.1 macrophages *in vitro*. As shown in Fig. 4, J774 macrophages do not have a predominant M2 phenotype, which are known to have a higher phagocytic capacity than M1 macrophages. It is possible that cube CNP were more readily phagocytosed by the M1-skewed J774 macrophages. However, alveolar macrophages are predominantly M2 in phenotype and have higher phagocytic capacity than M1 macrophages. This may lead to less nuanced phagocytosis of CNP, resulting in similar uptake of sphere and cube CNP by alveolar macrophages [48].

On the other hand, the percentage of nanoparticle + monocytes (Fig. 6g, Supplemental Figs. 4d–f), dendritic cells (Fig. 6h, Supplemental Figs. 5d–f), and neutrophils (Fig. 6i, Supplemental Figs. 6d–f) was significantly greater in mice that received sphere CNP versus those that received cube CNP, indicating that sphere and cube CNP are differentially taken up by immune cells. Cytospins of CNP-treated macrophages obtained from BAL indicate internalization of both sphere and cube CNP (Fig. 6k) as evident from clusters of nanoparticles. In addition, we observed that both the sphere and cube CNP-treated groups showed large cell size along with activated macrophage morphology compared to the untreated group.

Taken together, these data indicate that treatment with either sphere or cube CNP leads to the recruitment of important immune cell populations to the RSV-infected airways. Additionally, cube CNP are taken up with greater frequency by alveolar macrophages relative to other inflammatory cells recruited to the airspace following RSV infection. Alternatively, sphere CNP are taken up by alveolar macrophages, monocytes, and neutrophils to a similar extent. This is a critical feature of cube CNP that make it ideally suited for influencing macrophage activation whilst avoiding enhanced uptake and activation of inflammatory cells such as neutrophils, which are associated with RSV-mediated inflammation [49,50].

### 2.7. CNP treatment activates alveolar macrophages

Alveolar macrophages are sentinel immune cells in the lung that are important for regulating immune responses. Hence, we evaluated the activation of alveolar macrophages in RSV-infected mice following sphere and cube CNP treatment. Administration of cube CNP, but not sphere CNP, following RSV infection significantly increased the total number of $CD86^+$ alveolar macrophages (Fig. 7a, Supplemental Figs. 7a–c), while its MFI – a measure of CD86 expression on each cell – (Fig. 7b) was significantly increased following both sphere and cube CNP treatment when compared to untreated mice. Furthermore, treatment with cube CNP, but not sphere CNP, increased the total number of

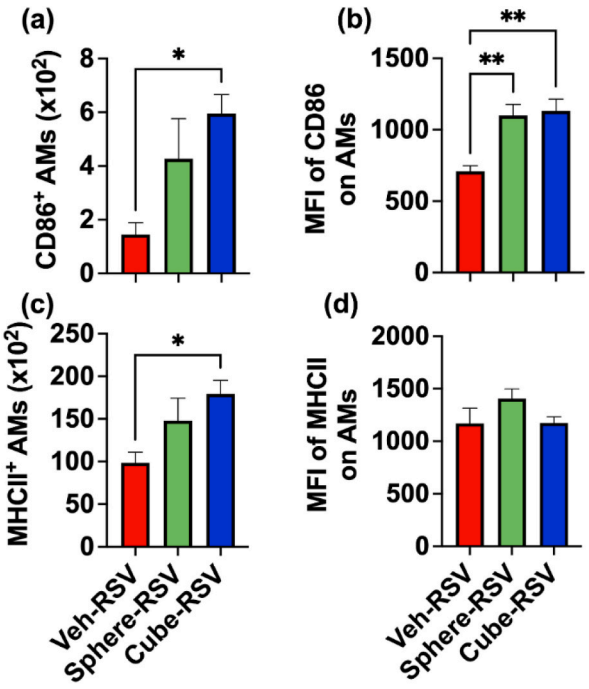


**Fig. 7. CNP treatment activates alveolar macrophages.** Mice were infected and treated as previously described. Total $CD86^+$ (a) and MHCII+ (c) alveolar macrophages were quantified via flow cytometry in the BAL of infected animals. Mean fluorescence intensity (MFI) of CD86 (b) and MHCII (d) on alveolar macrophages was determined via flow cytometry. Statistical significance was calculated using an unpaired *t*-test between groups. **p < 0.01.

$MHCII^+$ alveolar macrophages (Fig. 7c, Supplemental Figs. 7d–f). Neither cube nor sphere CNP treatment significantly altered the MFI of MHCII surface expression (Fig. 7d) when compared to untreated RSV-infected mice. Taken together, these data suggest that cube, more than sphere CNP alter the activation status of alveolar macrophages *in vivo* following RSV infection. MHC II is required for antigen presentation and CD86 is a critical co-stimulator molecule [42,51]; both are required for the activation of RSV-specific B and T cells. Thus, these data suggest that CNP effectively induce alveolar macrophage that will presumably activate the adaptive immune response to help clear RSV infection at later time points. This is of critical importance, as our previous studies have shown that infants, compared to adult mice, have a prolonged course of RSV infection [44].

## 3. Conclusion

This work highlights the effects of sphere and cube CNP in modulating reactive oxygen and reactive nitrogen species, in addition to their immunomodulatory activity. Cube CNP exhibited four-fold higher degree of crystallinity as compared to sphere CNP. *In vitro* macrophage assays demonstrated rapid intracellular uptake of both cube and sphere CNP. Changes in ROS and RNS levels revealed that the physicochemical properties of CNP can be a critical driver of differential cellular response as cube CNP reduced RSV-induced ROS levels significantly while maintaining RNS levels whereas sphere CNP increased RSV-induced RNS levels. Evaluation of surface marker expression suggested that the physicochemical properties of CNP influenced RSV-associated macrophage activation where cube CNP favored a more anti-viral M1 phenotype compared to sphere CNP. Similarly, cube CNP led to more pro-inflammatory cytokine production. However, both CNP led to a modest increase in IL-10, which is known to keep excess inflammation in check. Most interestingly, cube CNP showed selectivity for higher uptake by alveolar macrophages, a powerful attribute that could prevent off-target activation of other immune cells. Cube CNP exhibited greater

potency to induce alveolar macrophages compared to sphere CNP, suggesting cube CNP as a potential candidate with ability to activate an innate immune system.

## 4. Experimental sections

### 4.1. CNP synthesis

Sphere and Cube-shaped CNP were synthesized as reported earlier [19,20]. Briefly, cerium nitrate Ce $(NO_3)_3{\cdot}6H_2O$ (0.868 g, Acros Organics, Carlsbad, CA, USA) was dissolved in deionized water, which was then introduced into sodium hydroxide solution (6 M) in a drop-wise manner with continuous stirring to obtain cube-shaped CNP. Uniformity of the mixture was ensured by stirring for 30 min at room temperature. The mixture was exposed to hydrothermal treatment using a mini autoclave at 180°C for 24 h for cube CNP. The resulting CNP were washed, centrifuged, and re-suspended in purified water until the pH of the supernatant was neutral. The isolated particles were oven-dried overnight at 60 °C and were stored at 4 °C until further use.

Sphere CNP were synthesized using ultrasonication method [19,20]. Cerium nitrate Ce $(NO_3)_3{\cdot}6H_2O$ (5.0 g, Sigma Aldrich, USA) was dissolved in deionized water (100 mL) containing methoxy polyethylene glycol (mPEG) (5000 Da, 1.0 g, Acros Organics, USA). The solution was sonicated using pulse sonication by inserting a probe inside the cerium nitrate and mPEG solution mixture. Sodium hydroxide (NaOH) solution was introduced dropwise with continuous stirring and sonication until pH of 10 was reached. CNP suspension was allowed to settle down, the supernatant was discarded and CNP suspension was centrifuged. Collected CNP were washed several times with water until pH reached 7.4 following which it was washed with alcohol to remove the unbound/free mPEG. The CNP were then dried overnight at 100 °C.

### 4.2. FITC-CNP synthesis

CNP were functionalized with FITC in a two-step process. CNP were functionalized with amine as per method reported previously [19]. Briefly, CNP (2 mg/mL) were dispersed in anhydrous tetrahydrofuran (Acros Organics, USA) under an inert argon atmosphere using ultrasonication at room temperature for 90 min. 3-aminopropyltriethoxysilane (APTES) (Acros Organic, USA) was utilized to catalyze the functionalization through drop-wise addition to the CNP in 1:20 (CNP: APTES) molar ratio. The resulting CNP were acetone-washed and dried under ambient conditions for 24 h. FITC conjugation onto amine functionalized CNP was facilitated through dissolution of FITC and amine-functionalized CNP in dark conditions overnight.

### 4.3. Transmission electron microscopy (TEM)

A droplet of CNP dispersion was loaded on to the copper grids and imaged using JEOL 1011 transmission electron microscope (Joel, Tokyo, Japan) at an accelerated voltage of 80 kV.

### 4.4. X-ray diffraction

Dried CNP samples were analyzed using Bruker D8 Discover XRD (Bruker Corporation, Billerica, Massachusetts) at a generator voltage of 40 kV and current of 40 mA. The 2θ values were exported and plotted using GraphPad Prism 8 (GraphPad Software Inc., San Diego, CA). Crystallinity of the particles was calculated using Scherrer equation [52].

### 4.5. CNP suspension characterization

CNP were dispersed in MilliQ water (1 mg/mL stock suspension) using a probe sonicator (Sonic Dismembrator Model 500, Fisher Scientific, USA) for 20 min at 10% amplitude every 10s over a 20-min. To study the dispersibility of CNP in various buffers, the stock suspension was further diluted to make 25 μg/mL suspension in various buffers such as 4-(2-hydroxyethyl)-1-piperazineethanesulfonic acid (HEPES) and phosphate buffered saline (PBS). Hydrodynamic size and zeta potential were analyzed using Malvern ZEN 3600 Zetasizer (Malvern, UK). The effect of pH on CNP dispersibility was studied using HEPES at pH of 4.1, 6.1, and 7.1. The effect of serum on hydrodynamic particle size and zeta potential was studied using DMEM with and without 10% fetal bovine serum (FBS). ImageJ software version 1.53a (National Institute of health) was used to calculate the dimensions of 150 particles of all the shapes of cerium oxide nanoparticles.

### 4.6. Protein absorption assay

CNP suspension (50 μg/mL) were incubated in DMEM with 10% v/v of FBS at room temperature as described before [19]. After incubation, the protein-adsorbed CNP were separated by centrifuging at 13,200 rpm and washed with PBS. The hard corona of proteins was removed by sonicating the precipitate in Laemmli buffer. The CNP were vortexed in Laemmli buffer, boiled in hot water bath and separated by centrifugation at 13,200 rpm. Acrylamide gel was prepared for 2D sodium dodecyl sulfate polyacrylamide gel electrophoresis (SDS-PAGE). Fifteen microliter CNP suspension was loaded in each well along with the molecular marker for reference. Voltage of 120V was applied for 90 min. The gel was then stained for 2 h and then de-stained overnight. Gel Doc EZ Imager (BioRad Laboratories, Hercules, CA) was used to image the gel.

### 4.7. Cell culture

J774A1 mouse macrophage cells were maintained in complete culture media (DMEM supplemented with 10% FBS, 1% penicillin and streptomycin (Corning Inc., Corning, NY)) in T75 flasks in a humidified incubator at 37 °C and 5% $CO_2$. Culture was replenished with fresh media every 2 days, and cells were split at 70% confluence.

### 4.8. Cytocompatibility assay

Metabolic activity assay was used to determine cytocompatibility of CNP as described previously [53]. Briefly, J774A1 cells were exposed to different concentration of CNP (0, 5, 10, 20, 40, 80, 150 μg/mL) for 24 h at 37 °C, followed by incubation with alamarBlue® assay (Thermo Fisher Scientific, Waltham, MA) solution (10% v/v, 500 μL) in complete growth media for 4 h at 37 °C. The fluorescence intensity of reduced alamarBlue was then measured at an excitation/emission wavelength of 530/590 nm (Synergy HT, BioTek instruments, Winooski, VT, USA). The alamarBlue® solution in media was used as process control for background fluorescence correction. Further, macrophages that received alamarBlue® and media without CNP (0 μg/mL CNP, media only) were used as negative controls. The viability of CNP-treated macrophages was calculated using those without CNP treatment as 100% viability as per equation below, where RFU: relative fluorescence units.

$$\%\ \text{Viability} = \text{RFU}_{\text{CNP}} / \text{RFU}_{\text{Blank}} \times 100\% \quad \text{(Equation 1)}$$

### 4.9. CNP uptake studies

J774A1 macrophages were treated with FITC-tagged sphere and cube CNP (25 μg/mL) for 6 h at 37 °C followed by washing with sterile DPBS three times to remove CNP that were not taken up by the cells. Cells were fixed in 4% formaldehyde for 20–30 min, followed by nuclear staining with Hoechst 33,342 (10 μM, 1:500). Cellular uptake was studied using confocal laser scanning microscope (Olympus Fluoview 1000; Olympus Corporation, Tokyo, Japan). Z-stack images were captured with 5 μM thickness of each z-slice using 20× objective lens at

488 nm (FITC) and 405 nm (Hoechst) wavelengths. Data are presented as maximum intensity projection of the z-stack.

Corrected total cell fluorescence (CTCF) per cell was derived from confocal images using ImageJ software. Briefly, the area outside of cell was used to set background intensity. Cell area was selected to measure area and integrated density values. CTCF was calculated as per the equation below.

CTCF = Integrated Density – (Area of selected cell X Mean fluorescence of background readings)

### 4.10. Measurement of reactive oxygen species (ROS)

Macrophages ($0.1 \times 10^6$ cells/mL) were seeded in tissue culture treated 24-well plate and allowed to attach overnight. Macrophages were then infected with RSV Line 19 (RSV L19) at a multiplicity of infection (MOI) of 3 for 3 h, followed by treatment with sphere or cube CNP (25 μg/mL) for additional 6 or 12 h. The experimental design consisted of following groups of macrophages: 1) untreated, 2) RSV-infected, 3) sphere CNP, 4) RSV + sphere CNP, 5) cube CNP, and 6) RSV + cube CNP. The groups receiving RSV treatment were separately cultured in different well plates and incubated in separate incubators to avoid cross-contamination of CNP only groups with RSV. At the end of corresponding duration of incubation, macrophages were washed with DPBS and incubated with CellROX™ (Thermo Fisher Scientific, Waltham, MA) for 30 min, followed by washing with DPBS and the fluorescence intensity was measured at 488 nm using a microplate reader (Synergy HT, BioTek instruments, Winooski, VT, USA).

### 4.11. Measurement of reactive nitrogen species (RNS)

The extracellular RNS levels in macrophages were measured using Griess reagent (Promega, Madison, WI, USA) as per the manufacturer recommended protocol. The Griess reagent assay utilizes the chemical reaction between sulfanilamide and N-1-napthylethylenediamine dihydrochloride under acidic (phosphoric acid) conditions to detect nitrite ($NO2^-$) concentration secreted in the cell culture medium.

In order to accurately estimate nitrogen species, a standard curve was constructed using known concentrations of nitrite solution diluted in culture media according to the manufacturer's protocol. The experiment was conducted as explained under ROS measurement and the culture supernatant collected at the end of 6 or 12 h incubation was used for the RNS assay. Nitrate reductase co-factor and enzyme (10 μL each, Cayman Chemicals, Ann Arbor, MI) were mixed sequentially to the collected supernatant culture media (80 μL) using a Thermomixer R (Eppendorf, Germany) at 37 °C, 300 rpm for 2 h. Subsequently, Griess reagent sulfanilamide solution and NED solution were added (50 μL each) and the mixture was further incubated for 10 min to allow the colorimetric reaction to occur. Absorbance was measured at wavelength of 540/550 nm using a microplate reader (Synergy HT, BioTek instruments, Winooski, VT, USA). RNS values (μM) were interpolated from the standard curve.

### 4.12. M1 versus M2 J774A1 phenotype assessment

For macrophage phenotype assay, $1 \times 10^5$ J774A1 macrophages were seeded into 24-well plates and allowed to adhere overnight. Cells were then infected with RSV Line 19 (RSV L19) at a multiplicity of infection (MOI) of 3. At 3 h post-RSV infection, cells were treated with 25 μg/mL sphere, or cube CNP for an additional 6 or 24 h. For phenotyping of J774A1 macrophages, RSV-infected and/or nanoparticle-treated J774A1 macrophages were surface stained with antibodies against CD86 (GL1), CD80 (16-10A1), and CD206 (C068C2) for flow cytometric analysis. All antibodies were purchased from BioLegend (San Diego, CA), BD Biosciences (San Jose, CA) or eBiosciences (ThermoFisher Scientific, San Diego, CA). Samples were run on a BD LSRFortessa managed by the United Flow Core of the University of Pittsburgh. Data was analyzed using FlowJo V10 software (FLOWJO, LLC, OR). M1 macrophages were defined as $CD86^+$ $CD206^-$ or $CD80^+$ $CD206^-$ and M2 macrophages were defined as $CD86^-$ $CD206^+$ or $CD80^-$ $CD206^+$. Culture supernatants were assessed for M1 vs M2 cytokine secretion (TNFα, IL-10, and IL-12p70) using Bio-Plex Pro Mouse Cytokine Th1/Th2 Immunoassay (BioRad, Hercules, CA).

### 4.13. Mice, RSV infection, in vivo CNP treatment, and assessment of immune cell population

This study was carried out in strict accordance with the recommendations in the Guide for the Care and Use of Laboratory Animals of the National Institutes of Health. Mice were housed at The University of Pittsburgh Division of Laboratory Animal Resources. These animal experiments were approved by The University of Pittsburgh Institutional Animal Care and Use Committee (IACUC), approved protocol number 20047209 and mice were handled according to IACUC guidelines. All efforts were made to minimize animal suffering.

Adult female Balb/cJ mice (The Jackson Laboratory, Bar Harbor, ME) were infected with $5 \times 10^5$ pfu/gm RSV Line 19 (RSV L19) at 7–8 weeks of age, as previously described [54]. At 1- and 3-days post-infection, mice were intranasally administered 55 μg FITC-labeled sphere or cube CNP in 100 μL 10 mM HEPES pH = 4. Vehicle control animals received 100 μL of 10 mM HEPES pH = 4.

For *in vivo* assessment of immune cell populations, bronchoalveolar lavage (BAL) was processed and enumerated, as previously described [54]. For cytospins, BAL was diluted, and cells were spun onto glass slides prior to methanol fixation and staining with Diff-Quik (Dade International, Deerfield, IL) as previously described [55]. Images of alveolar macrophages were acquired using Olympus IX83 fluorescence microscope (Olympus Global, Center Valley, PA). For flow cytometry, BAL cells ($0.5–1x10^6$) were surface stained with antibodies against CD11c (HL3), CD11b (M1/70), Siglec F (E50-2440), F4/80 (T45-2342), CD206, Ly6G (1A8), CD86, and MHCII (M5/114.15.2). All antibodies were purchased from BioLegend (San Diego, CA), BD Biosciences (San Jose, CA) or eBiosciences (ThermoFisher Scientific, San Diego, CA). Alveolar macrophages were defined as $SiglecF^+$ $F4/80^+$ $CD206^+$ while monocytes were defined as $SiglecF^-$ $Ly6G^-$ $F4/80^+$ $CD206^-$. Dendritic cells were defined as $CD11c^+$ $MHCII^{hi}$ and neutrophils were defined as $SiglecF^-$ $Ly6G^+$. Samples were run on a BD LSRFortessa managed by the United Flow Core of the University of Pittsburgh. Data was analyzed using FlowJo V10 software (FLOWJO, LLC, OR).

### 4.14. Statistical analysis and preparation of graphical content

Experimental data are presented as mean ± standard deviation or mean ± standard error of mean as reported in the figure legends. Data across multiple groups were analyzed using one-way ANOVA or two-way ANOVA followed by Tukey's post-hoc analysis (GraphPad Prism 8, GraphPad Software Inc., San Diego, CA). The $p$ values less than 0.05 were considered as significant and annotated with asterisk. Graphical content was created using BioRender Web application.

## CRediT authorship contribution statement

**Akhil Patel:** Conceptualization, Validation, Formal analysis, Investigation, Data curation, Writing – original draft, Writing – review & editing, Visualization. **Jessica Kosanovich:** Conceptualization, Validation, Formal analysis, Investigation, Data curation, Writing – original draft, Writing – review & editing, Visualization. **Sameera Sansare:** Formal analysis, Investigation, Data curation, Writing – review & editing. **Sricharani Balmuri:** Formal analysis, Investigation, Writing – review & editing, Visualization. **Vinayak Sant:** Conceptualization, Validation, Writing – original draft, Writing – review & editing. **Kerry M. Empey:** Conceptualization, Methodology, Validation, Formal analysis, Investigation, Data curation, Writing – original draft, Writing –

review & editing, Visualization, Supervision, Project administration, Funding acquisition. **Shilpa Sant:** Conceptualization, Methodology, Validation, Formal analysis, Investigation, Data curation, Writing – original draft, Writing – review & editing, Visualization, Supervision, Project administration, Funding acquisition.

## Declaration of competing interest

Authors declare no conflicts of interests.

## Acknowledgements

We acknowledge funding support from the School of Pharmacy, University of Pittsburgh (SS), Brenneman Fund, University of Pittsburgh (KME), and Graduate Student Research Scholarship from the School of Pharmacy, University of Pittsburgh (AP). We thank Dr. Donna Stolz, Center for Biologic Imaging, University of Pittsburgh for access to TEM facility and Harini Venkata Krishnan for help with confocal image analysis. This work benefited from special BD LSRFORTESSATM funded by NIH 1S10OD011925-01 (PI: Borghesi).

## Appendix A. Supplementary data

Supplementary data to this article can be found online at https://doi.org/10.1016/j.bioactmat.2022.12.005.

## References

[1] G.L. Collaborators, Estimates of the global, regional, and national morbidity, mortality, and aetiologies of lower respiratory tract infections in 195 countries: a systematic analysis for the Global Burden of Disease Study 2015, Lancet Infect. Dis. 17 (11) (2017) 1133–1161.

[2] T. Shi, D.A. McAllister, K.L. O'Brien, E.A.F. Simoes, S.A. Madhi, B.D. Gessner, F. P. Polack, E. Balsells, S. Acacio, C. Aguayo, I. Alassani, A. Ali, M. Antonio, S. Awasthi, J.O. Awori, E. Azziz-Baumgartner, H.C. Baggett, V.L. Baillie, A. Balmaseda, A. Barahona, S. Basnet, Q. Bassat, W. Basualdo, G. Bigogo, L. Bont, R.F. Breiman, W.A. Brooks, S. Broor, N. Bruce, D. Bruden, P. Buchy, S. Campbell, P. Carosone-Link, M. Chadha, J. Chipeta, M. Chou, W. Clara, C. Cohen, E. de Cuellar, D.-A. Dang, B. Dash-yandag, M. Deloria-Knoll, M. Dherani, T. Eap, B. E. Ebruke, M. Echavarria, C.C. de Freitas Lázaro Emediato, R.A. Fasce, D.R. Feikin, L. Feng, A. Gentile, A. Gordon, D. Goswami, S. Goyet, M. Groome, N. Halasa, S. Hirve, N. Homaira, S.R.C. Howie, J. Jara, I. Jroundi, C.B. Kartasasmita, N. Khuri-Bulos, K.L. Kotloff, A. Krishnan, R. Libster, O. Lopez, M.G. Lucero, F. Lucion, S. P. Lupisan, D.N. Marcone, J.P. McCracken, M. Mejia, J.C. Moisi, J.M. Montgomery, D.P. Moore, C. Moraleda, J. Moyes, P. Munywoki, K. Mutyara, M.P. Nicol, D. J. Nokes, P. Nymadawa, M.T. da Costa Oliveira, H. Oshitani, N. Pandey, G. Paranhos-Baccalà, L.N. Phillips, V.S. Picot, M. Rahman, M. Rakoto-Andrianarivelo, Z.A. Rasmussen, B.A. Rath, A. Robinson, C. Romero, G. Russomando, V. Salimi, P. Sawatwong, N. Scheltema, B. Schweiger, J.A.G. Scott, P. Seidenberg, K. Shen, R. Singleton, V. Sotomayor, T.A. Strand, A. Sutanto, M. Sylla, M.D. Tapia, S. Thamthitiwat, E.D. Thomas, R. Tokarz, C. Turner, M. Venter, S. Waicharoen, J. Wang, W. Watthanaworawit, L.-M. Yoshida, H. Yu, H. J. Zar, H. Campbell, H. Nair, Global, regional, and national disease burden estimates of acute lower respiratory infections due to respiratory syncytial virus in young children in 2015: a systematic review and modelling study, Lancet 390 (10098) (2017) 946–958.

[3] J.A. Soto, N.M.S. Galvez, G.A. Pacheco, S.M. Bueno, A.M. Kalergis, Antibody development for preventing the human respiratory syncytial virus pathology, Mol. Med. 26 (1) (2020) 35.

[4] H. Nair, D.J. Nokes, B.D. Gessner, M. Dherani, S.A. Madhi, R.J. Singleton, K. L. O'Brien, A. Roca, P.F. Wright, N. Bruce, A. Chandran, E. Theodoratou, A. Sutanto, E.R. Sedyaningsih, M. Ngama, P.K. Munywoki, C. Kartasasmita, E. A. Simões, I. Rudan, M.W. Weber, H. Campbell, Global burden of acute lower respiratory infections due to respiratory syncytial virus in young children: a systematic review and meta-analysis, Lancet 375 (9725) (2010) 1545–1555.

[5] W. Aherne, T. Bird, S.D. Court, P.S. Gardner, J. McQuillin, Pathological changes in virus infections of the lower respiratory tract in children, J. Clin. Pathol. 23 (1) (1970) 7–18.

[6] T. Shibata, A. Makino, R. Ogata, S. Nakamura, T. Ito, K. Nagata, Y. Terauchi, T. Oishi, M. Fujieda, Y. Takahashi, M. Ato, Respiratory syncytial virus infection exacerbates pneumococcal pneumonia via Gas6/Axl-mediated macrophage polarization, J. Clin. Invest. 130 (6) (2020) 3021–3037.

[7] A. Rahal, A. Kumar, V. Singh, B. Yadav, R. Tiwari, S. Chakraborty, K. Dhama, Oxidative stress, prooxidants, and antioxidants: the interplay, BioMed Res. Int. 2014 (2014), 761264-761264.

[8] R. Vlahos, S. Selemidis, NADPH oxidases as novel pharmacologic targets against influenza A virus infection, Mol. Pharmacol. 86 (6) (2014) 747–759.

[9] W. Dröge, Free radicals in the physiological control of cell function, Physiol. Rev. 82 (1) (2002) 47–95.

[10] D.C. Munday, J.A. Hiscox, J.N. Barr, Quantitative proteomic analysis of A549 cells infected with human respiratory syncytial virus subgroup B using SILAC coupled to LC-MS/MS, Proteomics 10 (23) (2010) 4320–4334.

[11] M. Hu, M.A. Bogoyevitch, D.A. Jans, Impact of respiratory syncytial virus infection on host functions: implications for antiviral strategies, Physiol. Rev. 100 (4) (2020) 1527–1594.

[12] M. Jamaluddin, B. Tian, I. Boldogh, R.P. Garofalo, A.R. Brasier, Respiratory syncytial virus infection induces a reactive oxygen species-MSK1-phospho-Ser-276 RelA pathway required for cytokine expression, J. Virol. 83 (20) (2009) 10605–10615.

[13] W. MacNee, Oxidative stress and lung inflammation in airways disease, Eur. J. Pharmacol. 429 (1–3) (2001) 195–207.

[14] S.M. Castro, A. Guerrero-Plata, G. Suarez-Real, P.A. Adegboyega, G.N. Colasurdo, A.M. Khan, R.P. Garofalo, A. Casola, Antioxidant treatment ameliorates respiratory syncytial virus-induced disease and lung inflammation, Am. J. Respir. Crit. Care Med. 174 (12) (2006) 1361–1369.

[15] S.F. Dowell, Z. Papic, J.S. Bresee, C. Larrañaga, M. Mendez, A.L. Sowell, H.E. J. Gary, L.J. Anderson, L.F. Avendaño, Treatment of respiratory syncytial virus infection with vitamin A: a randomized, placebo-controlled trial in Santiago, Chile, Pediatr. Infect. Dis. J. 15 (9) (1996) 782–786.

[16] Y.M. Hosakote, T. Liu, S.M. Castro, R.P. Garofalo, A. Casola, Respiratory syncytial virus induces oxidative stress by modulating antioxidant enzymes, Am. J. Respir. Cell Mol. Biol. 41 (3) (2009) 348–357.

[17] M. Hu, M.A. Bogoyevitch, D.A. Jans, Subversion of host cell mitochondria by RSV to favor virus production is dependent on inhibition of mitochondrial complex I and ROS generation, Cells 8 (11) (2019) 1417.

[18] N. Zang, X. Xie, Y. Deng, S. Wu, L. Wang, C. Peng, S. Li, K. Ni, Y. Luo, E. Liu, Resveratrol-mediated gamma interferon reduction prevents airway inflammation and airway hyperresponsiveness in respiratory syncytial virus-infected immunocompromised mice, J. Virol. 85 (24) (2011) 13061–13068.

[19] Y. Xue, S.R. Balmuri, A. Patel, V. Sant, S. Sant, Synthesis, physico-chemical characterization, and antioxidant effect of PEGylated cerium oxide nanoparticles, Drug Deliv.Transl. Res. 8 (2) (2018) 357–367.

[20] Y. Xue, C. St Hilaire, L. Hortells, J.A. Phillippi, V. Sant, S. Sant, Shape-specific nanoceria mitigate oxidative stress-induced calcification in primary human valvular interstitial cell culture, Cell. Mol. Bioeng. 10 (5) (2017) 483–500.

[21] S.S. Lee, W. Song, M. Cho, H.L. Puppala, P. Nguyen, H. Zhu, L. Segatori, V. L. Colvin, Antioxidant properties of cerium oxide nanocrystals as a function of nanocrystal diameter and surface coating, ACS Nano 7 (11) (2013) 9693–9703.

[22] B. Stephen Inbaraj, B.-H. Chen, An overview on recent in vivo biological application of cerium oxide nanoparticles, Asian J. Pharm. Sci. 15 (5) (2020) 558–575.

[23] Y. Wu, H.T. Ta, Different approaches to synthesising cerium oxide nanoparticles and their corresponding physical characteristics, and ROS scavenging and anti-inflammatory capabilities, J. Mater. Chem. B (2021).

[24] N.Y. Spivak, N. Nosenko, N. Zholobak, A.B. Shcherbakov, A. Reznikov, O.g. S. Ivanova, V.K. Ivanov, Y.D. Tret'yakov, The nanocrystalline cerium dioxide raises the functional activity of genesial system of ageing males of rats, Nanosyst.: Phys. Chem. Math. 4 (1) (2013) 72–77.

[25] F. Pagliari, C. Mandoli, G. Forte, E. Magnani, S. Pagliari, G. Nardone, S. Licoccia, M. Minieri, P. Di Nardo, E. Traversa, Cerium oxide nanoparticles protect cardiac progenitor cells from oxidative stress, ACS Nano 6 (5) (2012) 3767–3775.

[26] M.B. Kolli, N. Manne, R. Para, S.K. Nalabotu, G. Nandyala, T. Shokuhfar, K. He, A. Hamlekhan, J.Y. Ma, P.S. Wehner, L. Dornon, R. Arvapalli, K.M. Rice, E. R. Blough, Cerium oxide nanoparticles attenuate monocrotaline induced right ventricular hypertrophy following pulmonary arterial hypertension, Biomaterials 35 (37) (2014) 9951–9962.

[27] M. Nyoka, Y.E. Choonara, P. Kumar, P.P.D. Kondiah, V. Pillay, Synthesis of cerium oxide nanoparticles using various methods: implications for biomedical applications, Nanomaterials 10 (2) (2020) 242.

[28] C. Pan, D. Zhang, L. Shi, J. Fang, Template-free synthesis, controlled conversion, and CO oxidation properties of CeO2 nanorods, nanotubes, nanowires, and nanocubes, Eur. J. Inorg. Chem. 15 (2008) 2429–2436, 2008.

[29] H.X. Mai, L.D. Sun, Y.W. Zhang, R. Si, W. Feng, H.P. Zhang, H.C. Liu, C.H. Yan, Shape-selective synthesis and oxygen storage behavior of ceria nanopolyhedra, nanorods, and nanocubes, J. Phys. Chem. B 109 (51) (2005) 24380–24385.

[30] T. Naganuma, Shape design of cerium oxide nanoparticles for enhancement of enzyme mimetic activity in therapeutic applications, Nano Res. 10 (1) (2017) 199–217.

[31] L. Qi, A. Sehgal, J.C. Castaing, J.P. Chapel, J. Fresnais, J.F. Berret, F. Cousin, Redispersible hybrid nanopowders: cerium oxide nanoparticle complexes with phosphonated-PEG oligomers, ACS Nano 2 (5) (2008) 879–888.

[32] J.J. Gulicovski, I. Bračko, S.K. Milonjić, Morphology and the isoelectric point of nanosized aqueous ceria sols, Mater. Chem. Phys. 148 (3) (2014) 868–873.

[33] M.A. Wells, A. Abid, I.M. Kennedy, A.I. Barakat, Serum proteins prevent aggregation of Fe2O3 and ZnO nanoparticles, Nanotoxicology 6 (2012) 837–846.

[34] Y.M. Hosakote, T. Liu, S.M. Castro, R.P. Garofalo, A. Casola, Respiratory syncytial virus induces oxidative stress by modulating antioxidant enzymes, Am. J. Respir. Cell Mol. Biol. 41 (3) (2009) 348–357.

[35] Y.M. Hosakote, P.D. Jantzi, D.L. Esham, H. Spratt, A. Kurosky, A. Casola, R. P. Garofalo, Viral-mediated inhibition of antioxidant enzymes contributes to the pathogenesis of severe respiratory syncytial virus bronchiolitis, Am. J. Respir. Crit. Care Med. 183 (11) (2011) 1550–1560.

[36] G. Franke, J. Freihorst, C. Steinmuller, W. Verhagen, S. Hockertz, M.L. Lohmann-Matthes, Interaction of alveolar macrophages and respiratory syncytial virus, J. Immunol. Methods 174 (1–2) (1994) 173–184.
[37] M. Rath, I. Muller, P. Kropf, E.I. Closs, M. Munder, Metabolism via arginase or nitric oxide synthase: two competing arginine pathways in macrophages, Front. Immunol. 5 (2014) 532.
[38] A. Predonzani, B. Cali, A.H. Agnellini, B. Molon, Spotlights on immunological effects of reactive nitrogen species: when inflammation says nitric oxide, World J. Exp. Med. 5 (2) (2015) 64–76.
[39] C. Bartholomew, J.N. Ihle, Retroviral insertions 90 kilobases proximal to the Evi-1 myeloid transforming gene activate transcription from the normal promoter, Mol. Cell Biol. 11 (4) (1991) 1820–1828.
[40] C. Bogdan, Nitric oxide and the immune response, Nat. Immunol. 2 (10) (2001) 907–916.
[41] P.M. Elks, S. Brizee, M. van der Vaart, S.R. Walmsley, F.J. van Eeden, S. A. Renshaw, A.H. Meijer, Hypoxia inducible factor signaling modulates susceptibility to mycobacterial infection via a nitric oxide dependent mechanism, PLoS Pathog. 9 (12) (2013), e1003789.
[42] S.W. Van Gool, P. Vandenberghe, M. de Boer, J.L. Ceuppens, CD80, CD86 and CD40 provide accessory signals in a multiple-step T-cell activation model, Immunol. Rev. 153 (1996) 47–83.
[43] E. Kinnear, L. Lambert, J.U. McDonald, H.M. Cheeseman, L.J. Caproni, J. S. Tregoning, Airway T cells protect against RSV infection in the absence of antibody, Mucosal Immunol. 11 (1) (2018) 249–256.
[44] K.M. Empey, J.G. Orend, R.S. Peebles Jr., L. Egana, K.A. Norris, T.D. Oury, J. K. Kolls, Stimulation of immature lung macrophages with intranasal interferon gamma in a novel neonatal mouse model of respiratory syncytial virus infection, PLoS One 7 (7) (2012), e40499.
[45] K.M. Eichinger, L. Egana, J.G. Orend, E. Resetar, K.B. Anderson, R. Patel, K. M. Empey, Alveolar macrophages support interferon gamma-mediated viral clearance in RSV-infected neonatal mice, Respir. Res. 16 (2015) 122.
[46] T. Hussell, A. Pennycook, P.J. Openshaw, Inhibition of tumor necrosis factor reduces the severity of virus-specific lung immunopathology, Eur. J. Immunol. 31 (9) (2001) 2566–2573.
[47] B.S. Graham, T.R. Johnson, R.S. Peebles, Immune-mediated disease pathogenesis in respiratory syncytial virus infection, Immunopharmacology 48 (3) (2000) 237–247.
[48] T. Roszer, Understanding the mysterious M2 macrophage through activation markers and effector mechanisms, Mediat. Inflamm. 2015 (2015), 816460.
[49] P.S. McNamara, P. Ritson, A. Selby, C.A. Hart, R.L. Smyth, Bronchoalveolar lavage cellularity in infants with severe respiratory syncytial virus bronchiolitis, Arch. Dis. Child. 88 (10) (2003) 922–926.
[50] M.L. Everard, A. Swarbrick, M. Wrightham, J. McIntyre, C. Dunkley, P.D. James, H. F. Sewell, A.D. Milner, Analysis of cells obtained by bronchial lavage of infants with respiratory syncytial virus infection, Arch. Dis. Child. 71 (5) (1994) 428–432.
[51] R.N. Germain, MHC-dependent antigen processing and peptide presentation: providing ligands for T lymphocyte activation, Cell 76 (2) (1994) 287–299.
[52] T. Sakthivel, S. Das, A. Kumar, D.L. Reid, A. Gupta, D.C. Sayle, S. Seal, Morphological phase diagram of biocatalytically active ceria nanostructures as a function of processing variables and their properties, Chempluschem 78 (12) (2013) 1446–1455.
[53] A. Patel, V. Sant, S. Velankar, M. Dutta, V. Balasubramanian, P. Sane, V. Agrawal, J. Wilson, L.C. Rohan, S. Sant, Self-assembly of multiscale anisotropic hydrogels through interfacial polyionic complexation, J. Biomed. Mater. Res. 108 (12) (2020) 2504–2518.
[54] K.M. Eichinger, J.L. Kosanovich, K.M. Empey, Localization of the T-cell response to RSV infection is altered in infant mice, Pediatr. Pulmonol. 53 (2) (2018) 145–153.
[55] K.M. Empey, M. Hollifield, B.A. Garvy, Exogenous heat-killed Escherichia coli improves alveolar macrophage activity and reduces Pneumocystis carinii lung burden in infant mice, Infect. Immun. 75 (7) (2007) 3382–3393.